Environmental Science & Technology

Article

pubs.acs.org/est

Effect of Bubbles and Silica Dissolution on Melter Feed Rheology during Conversion to Glass

José Marcial, Jaehun Chun,* Pavel Hrma, and Michael Schweiger

Pacific Northwest National Laboratory, P.O. Box 999, Richland, Washington 99352, United States

ABSTRACT: Nuclear-waste melter feeds are slurry mixtures of wastes with glass-forming and glass-modifying additives (unless prefabricated frits are used), which are converted to molten glass in a continuous electrical glass-melting furnace. The feeds gradually become continuous glass-forming melts. Initially, the melts contain dissolving refractory feed constituents that are suspended together with numerous gas bubbles. Eventually, the bubbles escape, and the melts homogenize and equilibrate. Knowledge of various physicochemical properties of the reacting melter feed is crucial for understanding the feed-to-glass conversion that occurs during melting. We studied the melter feed viscosity during heating and correlated it with the volume fractions of dissolving quartz (SiO_2) particles and the gas phase. The measurements were performed with a rotating spindle rheometer on the melter feed heated at 5 K/min, starting at several different temperatures. The effects of undissolved quartz particles, gas bubbles, and compositional inhomogeneity on the melter feed viscosity were determined by fitting a linear relationship between the logarithm of viscosity and the volume fractions of suspended phases.

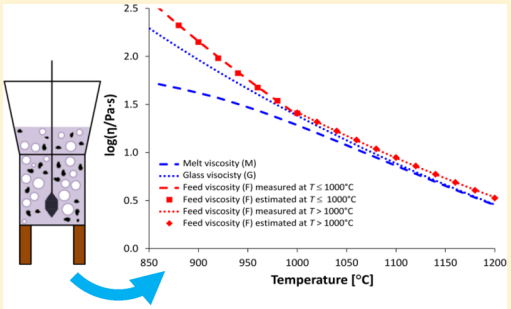

Feed viscosity as a function of temperature from trend lines, model estimates, average transient glass-forming melt viscosity, and final glass viscosity

INTRODUCTION

The "cold cap" refers to a floating layer of "cold" melter feed on top of a pool of "hot" molten glass in a continuous electrical (Joule-heated) glass-melting furnace (a "melter"). In nuclear waste glass processing at the Waste Treatment and Immobilization Plant (WTP) currently under construction at the Hanford Site in Washington State, USA, the feed, a slurry mixture of waste with glass-forming and glass-modifying additives, will be continuously charged onto the cold cap that covers 90−100% of the melt surface. As the melter feed moves down through the cold cap, its temperature increases and the feed undergoes chemical reactions and phase transitions until it is converted to molten glass.[1−3]

The waste itself contains 40−60 elements existing as water-soluble salts, amorphous gels, and crystalline minerals. Conversion to glass proceeds over a wide range of temperatures spanning formation of a molten salt phase that reacts with feed solids, turning them into intermediate products and ultimately the glass-forming melt.[4−6] Such physicochemical processes take place in melter feeds whether the glass-forming and glass-modifying additives were directly mixed with wastes or premelted in the form of glass frit. This has been demonstrated in high-temperature X-ray diffraction in situ studies[7] for frit-based melter feeds of the Defense Waste Processing Facility at Savannah River Site, South Carolina, USA.

Evolved gases escape through open pores in the cold cap until the temperature increases to ∼700−800 °C, but a fraction of residual gases can be trapped in the transient glass-forming melt and cause foaming. Foam in the cold cap reduces heat transfer from molten glass into the cold cap, thus decreasing the melting rate.[8,9]

Apart from gas bubbles, the continuous glass-forming melt also contains various particles of dissolving feed solids and intermediate crystalline phases. Understanding the evolution of physical and mechanical properties of the melter feed turning to molten glass is crucial for both feed formulation and modeling of the feed-to-glass conversion. For example, the type of feed materials and the grain size of silica particles were shown to affect the melter feed behavior.[10,11]

Bubble formation and melt foaming occur in both commercial and waste glass melters during the final stages of the feed-to-glass conversion process. Studies have been conducted to address the morphology and properties of foam systems,[9,12−17] and waste-glass viscosity as a function of temperature and composition has been mathematically modeled.[18,19] However, no study has been rigorously performed for rheological properties of melter feeds containing suspended solid particles and gas bubbles with fractions that vary as the conversion progresses.

In this work, we focus on the melter feed viscosity during the feed-to-glass conversion using a feed with glass-forming and glass-modifying additives. Variations of gas and solid (quartz) inclusions associated with conversion progress were analyzed and employed as the key variables. The following sections provide background and define relationships for analysis, describe the experiments, and present and discuss the results.

Received: April 14, 2014
Revised: September 8, 2014
Accepted: September 17, 2014
Published: September 17, 2014

dx.doi.org/10.1021/es5018625 | Environ. Sci. Technol. 2014, 48, 12173−12180

BACKGROUND AND RELATIONSHIPS FOR ANALYSIS

This work was performed using a melter feed (A0) formulated to vitrify a high-alumina high-level waste with the composition shown in Table 1. Quartz particles 75 μm in diameter were used as the silica source. Table 2 shows the glass composition. This glass was originally designed for the WTP.[20]

Table 1. Melter Feed Composition (g kg^{-1} Glass)

chemical	mass (g)
$Al(OH)_3$	367.50
H_3BO_3	269.83
CaO	60.80
$Fe(OH)_3$	73.83
Li_2CO_3	88.30
$Mg(OH)_2$	1.70
NaOH	99.53
SiO_2	305.03
$Zn(NO_3)_2{\cdot}4H_2O$	2.67
$Zr(OH)_4{\cdot}0.654H_2O$	5.50
Na_2SO_4	3.57
$Bi(OH)_3$	12.80
Na_2CrO_4	11.13
KNO_3	3.03
$NiCO_3$	6.33
$Pb(NO_3)_2$	6.17
$Fe(H_2PO_2)_3$	12.43
NaF	14.73
$NaNO_2$	3.40
$Na_2C_2O_4{\cdot}3H_2O$	1.30
total	1349.6

Table 2. Composition of Glass Used in This Study and First-Order Component Coefficients of Viscosity

component	mass fraction	10^{-4} B_i (K)
Al_2O_3	0.2407	3.506
B_2O_3	0.1522	0.352
CaO	0.0609	0.558
Fe_2O_3	0.0592	1.565
Li_2O	0.0358	−3.937
MgO	0.0012	1.184
Na_2O	0.0961	−0.031
SiO_2	0.3057	3.001
ZnO	0.0008	1.179
ZrO_2	0.0040	2.712
Bi_2O_3	0.0115	1.361
Cr_2O_3	0.0052	1.003
K_2O	0.0014	0.877
NiO	0.0040	0.397
PbO	0.0041	1.036
P_2O_5	0.0106	2.631
F	0.0067	−0.437

Because $\rho_g \ll \rho_c$, where ρ_g is the gas density and ρ_c is the continuous phase density (the melt with solid inclusions), the volume fraction of gas phase (porosity), φ_g, is $\varphi_g \approx (1 - \rho_b/\rho_c)$, where ρ_b is the bulk density. The bulk density is related to experimentally determined variables as

$$\rho_b = \frac{mV_0}{m_0V}\rho_{b,0} \tag{1}$$

where m is the sample mass, V is the sample volume, and subscript 0 indicates room temperature.

The mass fraction of dissolved quartz in the transient glass-forming melt was represented using an nth-order kinetic equation[21]

$$\frac{dx_s}{dT} = \frac{A_s}{\beta}(1 - x_s)^{\tilde{m}}\exp\left(-\frac{B_s}{T}\right) \tag{2}$$

where x_s is the dissolved quartz fraction ($0 < x_s < 1$), T is the temperature in K, A_s is the pre-exponential factor, $\tilde{m}$ is the (apparent) reaction order, β is the (constant) heating rate ($\beta \equiv dT/dt$), and B_s is the activation energy normalized by the gas constant. The numerical values of the coefficients for $\beta = 5$ K min^{-1} and A0 feed are $A_s = 2.33$ s^{-1}, $\tilde{m} = 1.33$, and $B_s = 8763$ K. These values were obtained by fitting eq 2 to X-ray diffraction data.[21]

The mass fraction of undissolved quartz in the melt is $g_s = g_{s0}(1 - x_s)$, where g_{s0} is the silica mass fraction in the final glass ($g_{s0} = 0.305$). The volume fraction of undissolved quartz, φ_s, is then

$$\varphi_s = \frac{1}{1 + \frac{\rho_s}{\rho_m}\left(\frac{1}{g_s} - 1\right)} \tag{3}$$

where ρ_s is the quartz density (2500 kg m^{-3})[22] and ρ_m is the melt density (2600 kg m^{-3}).

The viscosity of molten glass, η, is a function of temperature. For $\eta < 10^3$ Pa s, the $\eta(T)$ function has the Arrhenius form, $\eta = A\exp(B/T)$, where A is the pre-exponential factor ($A = -12.51$) and B is the activation energy for viscous flow,[23] which is a function of glass composition. For a reasonably small composition region,[18,19] $B = \sum_{i=1}^{N} B_i g_i$, where B_i is the ith component coefficient, g_i is the ith component mass fraction, and N is the number of components.

The fraction of silica in the glass-forming melt varies as the quartz particles dissolve. Recollecting that $\sum_{i=1}^{N} g_i = 1$ and neglecting minor solids and inhomogeneities, the activation energy of the transient glass-forming melt (B_M) depends on the mass fraction of the dissolved silica as follows:

$$B_M = (B_G - B_s g_{s0})\frac{1 - g_s}{1 - g_{s0}} + B_s g_s \tag{4}$$

where B_G is the activation energy of the homogeneous glass with all quartz dissolved and B_s is the component coefficient for quartz (SiO_2). The component coefficients for viscosity are listed in Table 2 together with the glass composition used in this study. Accordingly, $B_G = 1.998 \times 10^4$ K and $B_s = 3.001 \times 10^4$ K.

If the transient glass-forming melt were homogeneous and contained undissolved quartz as the only solid inclusion, its viscosity would be $\eta_M = A\exp(B_M/T)$. In reality, with the additive-containing feed, the transient glass-forming melt contains minor solid inclusions, mainly tiny crystals of spinel,[21] and dissolving quartz particles are surrounded by layers containing high fractions of silica.[11] The glass-forming melt within these layers has a high viscosity, whereas the viscosity of the rest of the melt is substantially lower.

According to Einstein's equation, the viscosity of a dilute suspension[24,25] is proportional to the volume fractions of gaseous and solid inclusions. The transient glass-forming melt in the reacting feed is far from dilute; it contains up to 20 vol % quartz and up to 80 vol % gas bubbles. Therefore, the viscosity

versus the inclusion content will have a different type of relationship. Because of the highly complex reacting feed mixture, equations proposed for dispersion of colloidal particles (such as the Krieger–Dougherty equation)[25] and/or bubbly magmas[26] do not fit experimental data for the reacting feed viscosity (η_F). As a first approximation, we tried an exponential relationship in the form

$$\log \frac{\eta_F}{\eta_M} = f_0 + f_s\varphi_s + f_g\varphi_g \quad (5)$$

where f_s and f_g are the coefficients for the influence of quartz and gas phase (bubbles) on the melting feed viscosity and f_0 is the coefficient accounting for other effects, such as the presence of tiny crystals (spinel), glass-forming melt local compositional inhomogeneity connected with the quartz dissolution process, and the nonuniform temperature field in the sample. Although the tiny crystals may have a negligible effect on viscosity, they can influence bubble behavior because solid inclusions interfere with bubble coalescence.[27,28] The effect of nonuniformity in the temperature field is examined in the Discussion section.

EXPERIMENTAL SECTION

As described by Schweiger et al.,[11] the simulated melter feed was prepared in the form of slurry that was dried, crushed into powder, and placed in an oven at 105 °C overnight. Thermogravimetric analysis (TGA, model SDT-Q600, TA Instruments, New Castle, DE, USA) was performed to obtain the mass change versus temperature for calculating the bulk density of the feed sample. The density of the continuous phase (ρ_c) was measured using a Micromeritics AccuPyc II 1340 gas pycnometer at room temperature. At the heat treatment temperature, the density is typically ~10% lower. The volumetric expansion of the feed samples was measured with cylindrical pellets.[29] TGA and volumetric expansion tests provided the m/m_0 and V/V_0 ratios (with a typical relative standard deviation of ~5–6%) to obtain the bulk density using eq 1.

Figure 1 provides a schematic of the experimental setup for the viscosity measurement, which was performed with ~125-g powder-feed samples placed in a platinum crucible containing a spindle at the appropriate height inside the furnace; these conditions are similar to those specified for rheological measurements with vanes.[30] The sample was heated at 5 K min^{-1} from room temperature to 1100 °C. Measurements started when the instrument thermocouple reached target temperatures (870, 900, 930, or 990 °C). The spindle was rotated at 0.3 rpm for the 870, 900, and 930 °C trials and at 0.9 rpm for the 990 °C trial. Data were obtained using DilaSoft II software from Theta Industries. Data acquisition occurred in 6-s intervals (the viscosity was measured at every 0.5 °C increment at 5 K min^{-1}).

Raw data were torques, which were converted into viscosities using the formula $\eta = T_q F_{sp}/\omega$. Here, T_q and ω denote the measured torque and angular velocity, respectively. F_{sp}, the spindle factor, was obtained from the average of spindle factors over a temperature range relevant to the measurement at a given angular velocity, compared with known viscosities of glass standard reference materials.[31] Using the A0 glass as the relevant material, the spindle factors at 0.3 and 0.9 rpm were found to be 1.785 and 3.35, respectively.

A second Type-S thermocouple was inserted beneath the crucible to determine the temperature. To assess the temperature at the spindle, a mullite-sheathed, Type-S thermocouple was inserted into the feed 13 mm from the crucible bottom (approximately the center point of the spindle). The crucible with feed (without the spindle) was heated at 5 K min^{-1}.

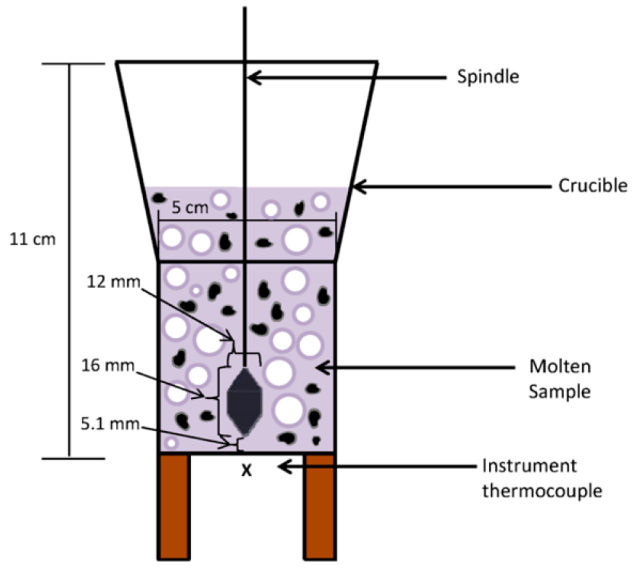

Figure 1. Schematic of the viscosity measurement setup.

RESULTS

Figure 2 shows the volume fraction of undissolved quartz, via eqs 2 and 3, as a function of temperature. Figure 3 shows the relative feed volume, V/V_0; after the glass-forming melt became continuous at ~750 °C, V/V_0 sharply increased due to trapped

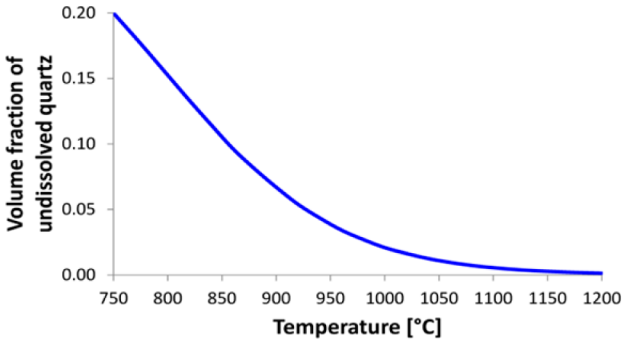

Figure 2. Volume fraction of undissolved quartz at T > 750 °C, eqs 2 and 3

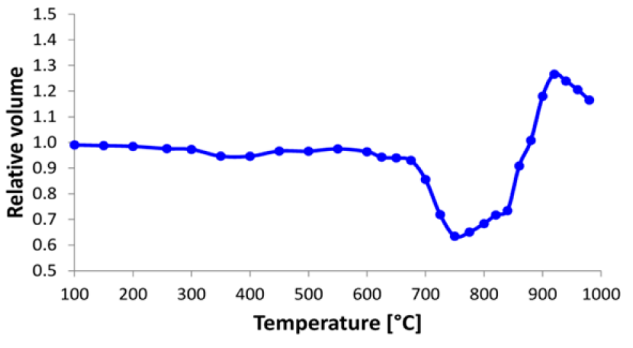

Figure 3. Relative volume of feed versus temperature.

dx.doi.org/10.1021/es5018625 | Environ. Sci. Technol. 2014, 48, 12173–12180

evolved gases.[29] The volume decrease after ~930 °C is attributed to coalescence and bursting of bubbles as viscosity decreased. Figure 4 shows the continuous-phase density

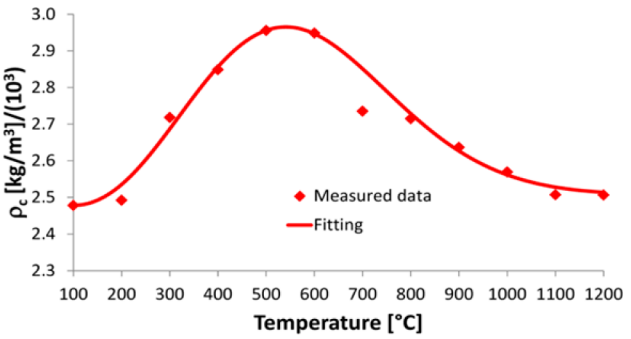

Figure 4. Continuous-phase density (data and fitting curve) versus temperature to which feed samples were heated at 5 K/min; density was measured on quenched feed samples.

measured on quenched samples as a function of the temperature to which the feed was heated at 5 K min^{-1}. Data were fitted using the approximation function

$$\rho_c = \rho_{c0} + \rho_{c1}\tan^{-1}\left(\frac{T - T_1}{T_2}\right) + a(T - T_3)^2\exp\left[-\left(\frac{T - T_4}{T_5}\right)^2\right] \quad (6)$$

where ρ_{c0} = 2492 kg m^{-3}, ρ_{c1} = 10.6 kg m^{-3}, T_1 = 534 °C, T_2 = 123 °C, T_3 = 100 °C, T_4 = 184 °C, T_5 = 389 °C, and a = 5.647 × 10^{-3} kg m^{-3} K^{-2}. The density increase below ~550 °C can be attributed to the disappearance of molten salts from the feed (carbonates, nitrates, and nitrites react with other feed constituents, releasing NO_x and CO_x), whereas the decrease at higher temperatures is related to the change of materials from crystalline to an amorphous state. The volume fraction of gas phase (Figure 5) was calculated from the bulk density at 25 °C ($\rho_{b,0}$ = 970 kg m^{-3}), the mass change from TGA, the volume expansion, and ρ_c.

Figure 6 shows measured data for the melting feed viscosity. Data obtained from measurements at different starting temperatures demonstrate that spindle rotation had a negligible effect on sample viscosity. Non-Newtonian behavior, such as a shear rate-dependent viscosity, was not observed; the fraction of spinel crystals was too small to induce a non-Newtonian

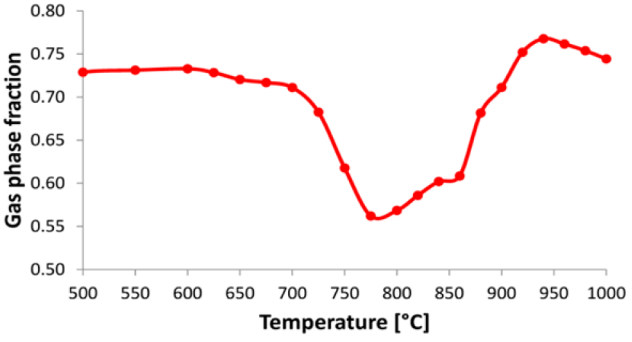

Figure 5. Gas phase fraction versus temperature to which feed samples were heated at 5 K/min.

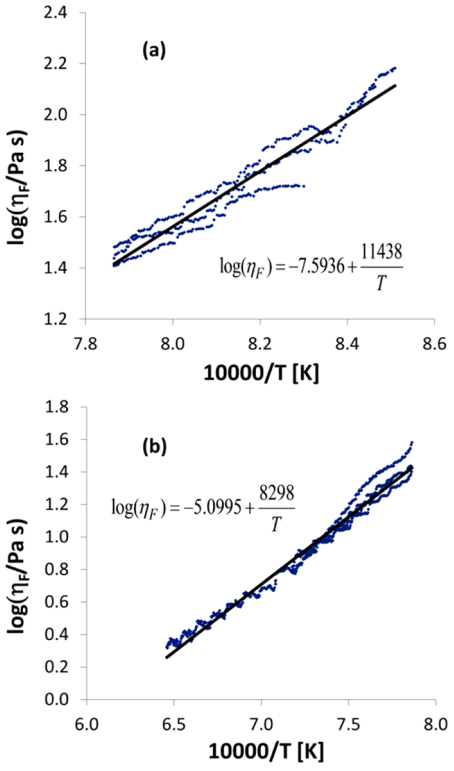

Figure 6. Log feed viscosity versus inverse temperature for (a) $T \leq$ 1000 °C and (b) $T >$ 1000 °C, and the trend lines.

response. As Figure 6 shows, the $\log(\eta_F)$ versus T^{-1} line changes slope at ~1000 °C, the temperature at which foam collapses. Foam collapse in heated feed is rapid. Experimental studies with commercial and waste glasses[8,9,32] indicate that foam collapse is preceded by internal coalescence of bubbles into increasingly larger cavities that eventually open, allowing the gas escape to the atmosphere. The trend lines in Figure 6,

$$\log(\eta_F) = A_F + \frac{B_F}{T} \quad (7)$$

represent two sets of data with the coefficients A_F = −7.5936 and B_F = 11438 K at $T \leq$ ~1000 °C, and A_F = −5.0995 and B_F = 8298 K at $T >$ ~1000 °C (η_F is in Pa s and T is in K).

Figure 7 compares three viscosity-temperature functions, $\eta_G(T)$, $\eta_M(T)$, and $\eta_F(T)$, plotted as $\log(\eta)$ versus T^{-1}. As expected, $\eta_F > \eta_G > \eta_M$ for the entire interval of temperatures. Following from eqs 2 and 4, the $\eta_G(T)$ and $\eta_M(T)$ functions merge as temperature increases and $g_s \rightarrow g_{s0}$ (solid silica is dissolved and the melt becomes homogeneous). Understandably, the difference between η_F and η_M is large initially (at 850 °C) and decreases until T = 980 °C. Then, rather unexpectedly, the $\eta_F(T)$ and $\eta_M(T)$ functions become virtually parallel at $T >$ 980 °C. This can be attributed to residual quartz grains, residual bubbles, persisting silica-rich inhomogeneities that take a long time to attenuate, and the nonuniform temperature in the sample resulting from finite heat conductivity of the sample (see Discussion) (i.e., the temperature gradient between the crucible and the spindle).

The first attempt to fit data to eq 5 by least-squares analysis applied separately for two temperature ranges, $T \leq$ 980 °C and $T >$ 980 °C, failed to yield reasonable values of the coefficients. The quartz content and the gas content probably were not independent. Indeed, a linear correlation between the quartz

dx.doi.org/10.1021/es5018625 | Environ. Sci. Technol. 2014, 48, 12173−12180

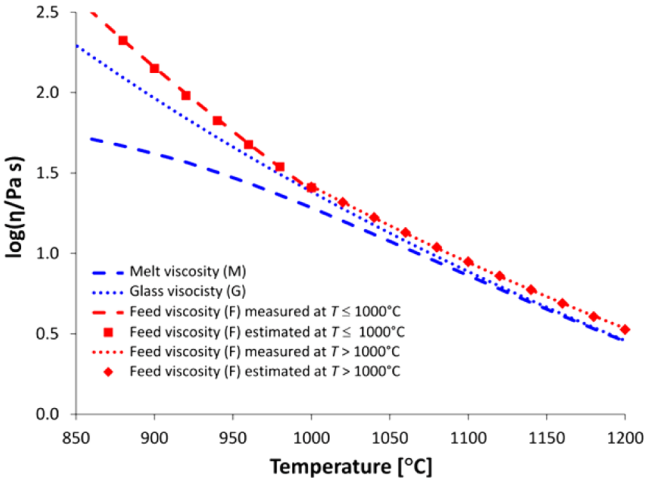

Figure 7. Log feed viscosity versus temperature: trend lines (shown in Figure 6), model estimates, eq 5, average transient glass-forming melt viscosity (η_M), and final glass viscosity (η_G).

and the gas contents, $\varphi_g = 0.38-0.45\varphi_s$ ($R^2 = 0.986$) was found in the temperature interval between 800 and 950 °C. Thus, because φ_g and φ_s were not independent and their individual effects could not be distinguished, we simplified eq 5 to

$$\log\left(\frac{\eta_F}{\eta_M}\right) = f_0 + f_{sg}\varphi_s \tag{8}$$

where the subscript sg indicates that both the gas phase and undissolved quartz (including the high-silica concentration layers) jointly influence viscosity.

The f_0 coefficient remains independent. Although the extent of silica-rich inhomogeneity is related to the quartz content, a direct proportionality can hardly be expected because the fraction of high-silica concentration layers in the melt increases as the fraction of solid silica decreases, and high-silica inhomogeneities persist after quartz particles are dissolved. Also, the f_0 coefficient involves other phenomena, such as the effect of minor crystalline phases and nonuniform temperature.

Least squares fitting of eq 8 to data resulted in the following coefficient values: $f_0 = -0.058$ and $f_{sg} = 8.822$ at $T \leq 980$ °C ($R^2 = 0.999$), and $f_0 = 0.068$ and $f_{sg} = 3.141$ at $T > 980$ °C ($R^2 = 0.999$). These values make sense because relatively thin high-silica concentration layers allow the bulk of the transient glass-forming melt to be less viscous at $T \leq 980$ °C, which explains why f_0 is negative. At $T > 980$ °C, the high-silica concentration layers would expand because of faster diffusion and would tend to overlap, creating a high-viscosity network of inhomogeneity; this resulted in a positive f_0. Simultaneously, bubbles and quartz particles are disappearing from the melt. Because they decrease in size, they affect viscosity to a lesser extent as reflected in a smaller value of f_{sg} at $T > 980$ °C. The persistence of the difference between the $\eta_F(T)$ and $\eta_M(T)$ functions at increasingly high temperatures can be attributed to the temperature gradient; the decreasing temperature in the direction from the crucible wall to the spindle at the center implies that the viscosity becomes higher in that direction.

Equation 8 can be rewritten as $\eta_F = K_{sg}\eta_M$, where K_{sg} is a ratio of the feed viscosity to the average transient melt viscosity, related to the fitting coefficients by $\log(K_{sg}) = f_0 + f_{sg}\varphi_s$. As Figure 8 shows, K_{sg} decreases from ~50 at 750 °C to nearly 1 at $T > 980$ °C.

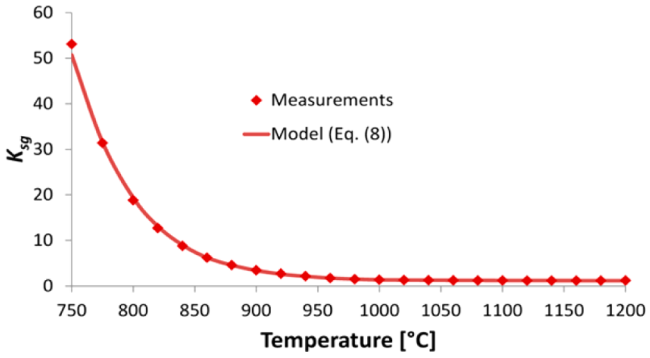

Figure 8. K_{sg} versus temperature from measured data and the model, eq 8. Note $R^2 = 0.999$.

DISCUSSION

Temperature Gradient and Its Impact on Spindle Factor. Viscosity measurements are typically taken at a constant temperature after the system is thermally equilibrated and steady state is established. However, for the reacting melter feed, in which the conversion process is a function of temperature and time, or temperature and heating rate, β, (provided β is constant), the measurement must be performed while the temperature is increasing. Then, because of the finite heat conductivity of the sample with the appreciable gap between the spindle and crucible (Figure 1), a temperature difference between the spindle and the crucible surfaces is unavoidable. However, the difference in the conversion degree over the gap between the spindle surface and the crucible is miniscule in comparison.

Here we assess the effect of the temperature difference between the spindle and crucible on the spindle factor. Consider a viscous fluid between two concentric cylinders; a motionless outer cylinder with the radius R_2 and temperature T_2, and a rotating inner cylinder with the radius R_1, temperature T_1, and angular velocity ω. In the case of steady-state laminar flow, fluid movement is circular so all velocity components other than a tangential velocity component of the fluid (v_θ) are zero with no variation in the angular and axial directions ($\partial/\partial\theta = 0$ and $\partial/\partial z = 0$). The equation of motion in the angular direction becomes[33]

$$0 = \frac{1}{r^2}\frac{d}{dr}(r^2\tau_{r\theta}) \tag{9}$$

with boundary conditions

$$v_\theta = \omega R_1 \text{ at } r = R_1;\ v_\theta = 0 \text{ at } r = R_2$$

The tangential stress is

$$\tau_{r\theta} = -\eta(r)r\frac{d}{dr}\left(\frac{v_\theta}{r}\right) \tag{10}$$

Note that viscosity is a function of the radial position. It is lower at the outer cylinder, increases in the direction to the inner cylinder as mentioned before, and can be approximated as

$$\eta(r) = \hat{A}r^{-n} \tag{11}$$

where $\hat{A}$ and n are positive constants. From eq 11, one obtains $n = -(d\ln\eta/d\ln r)$. Using the temperature dependence on the viscosity in the form $\eta(T) = \exp(A+B'/T)$, we obtain

$$n = r\left(\frac{B'}{T^2}\right)\frac{dT}{dr} \tag{12}$$

dx.doi.org/10.1021/es5018625 | Environ. Sci. Technol. 2014, 48, 12173−12180

The torque on the inner cylinder is

$$T_q|_{r=R_1} = 2\pi R_1 L(\tau_{r\theta})_{r=R_1} R_1 \quad (13)$$

where $(\tau_{r\theta})_{r=R1}$ and L denote the tangential stress at the inner cylinder and the length of the cylinder, respectively. Solving the equation of motion with eq 11 leads to the following expression for the tangential velocity component of the fluid:

$$v_\theta = r\omega\left[\frac{r^{n-2} - R_2^{n-2}}{R_1^{n-2} - R_2^{n-2}}\right] \quad (14)$$

Incorporating eq 14 into eq 10, the torque can be represented by

$$\tau_{r\theta} = \frac{\eta(r)\omega(2-n)r^{n-2}}{R_1^{n-2} - R_2^{n-2}} \quad (15)$$

To evaluate the tangential stress and torque on the inner cylinder, the variation of temperature with the radial position should be determined (eq 12). By using the energy transport equation with boundary conditions $T = T_1$ at $r = R_1$ and $T = T_2$ at $r = R_2$, the temperature profile is

$$T = T_1 + \Delta T\frac{\ln(r/R_1)}{\ln(R_2/R_1)} \quad (16)$$

where $\Delta T = T_2 - T_1$. Note that eq 16 is identical to the temperature profile for stationary concentric cylinders with the same boundary conditions; this is only possible when the Brinkman number, $Br = \eta\varpi^2R_2^2/k\Delta T$, where k is the thermal conductivity of the fluid, and a geometric factor, $F_R = (R_1/R_2)^4/(1-(R_1/R_2)^2)^2)$, are small.[33] Our situation falls into this case, based on typical values for our sample ($k \sim 2$ W m^{-1} K^{-1}, $\eta \sim$ 100 Pa s, and $B' \sim 2 \times 10^4$ K)[19,34] and viscometer ($\Delta T \sim 30$ K, $R_1 = 6$ mm, $R_2 = 25$ mm, and $\omega = 5 \times 10^{-3}$ s^{-1}).

Combining eqs 15 and 16 with eqs 12 and 13, the torque on the inner cylinder can be represented as

$$T_q|_{r=R_1} = 2\pi R_1^{n(R_1)} L\frac{\eta(R_1)\omega(2-n(R_1))}{R_1^{n(R_1)-2} - R_2^{n(R_1)-2}} \quad (17)$$

with

$$n(R_1) = \left(\frac{B'}{T_1^2}\right)\frac{\Delta T}{\ln(R_2/R_1)} \quad (18)$$

Consequently, the spindle factor on the inner cylinder is

$$F_{sp}|_{r=R_1} = \frac{\eta(R_1)\omega}{T_q|_{r=R_1}} = \frac{R_1^{n(R_1)-2} - R_2^{n(R_1)-2}}{2\pi L R_1^{n(R_1)}(2-n(R_1))} \quad (19)$$

Figure 9 illustrates the variation of the spindle factor as a function of ΔT at $T_1 = 850$, 1000, and 1200 °C, based on the viscometer radii and typical experimental conditions. A relative change of spindle factor, defined by the change of the spindle factor compared to the spindle factor with zero temperature difference, was used to eliminate the effect of cylinder length. As shown in Figure 9, the spindle factor varies appreciably in the 0 to 60 °C temperature difference range; the relative changes increase with increasing ΔT. Considering a typical ΔT (~ 20–40 °C), this demonstrates that using the predetermined uniform spindle factor inherently involves an appreciable uncertainty in the viscosity data, owing to the temperature difference. Furthermore, such uncertainty becomes more significant in viscosity measurements at lower temperatures.

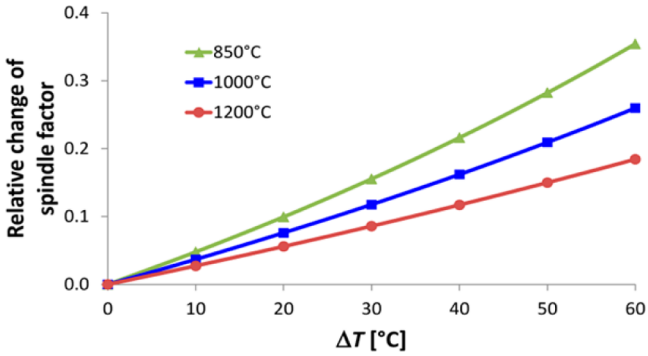

Figure 9. Relative changes in spindle factor as a function of temperature difference between spindle and crucible for three different temperatures on the spindle: 850, 1000, and 1200 °C.

Effect of Buoyancy of Gas Bubbles on Feed Viscosity at High Temperatures. At higher temperatures (such as $T >$ 1100 °C), the undissolved quartz content is negligible, as shown in Figure 2. Consequently, a change in the feed viscosity resulting from undissolved quartz is unlikely. However, local high-viscosity inhomogeneities prevail and take considerable time to attenuate. They are partly responsible for a consistent deviation of the measured viscosity (η_F) from that of the final glass (η_G) and the transient glass-forming melt (η_M), shown in Figure 7. Undoubtedly, the temperature gradient influences viscosity data, especially at high temperatures at which other nonuniformities are mostly attenuated.

Another possible reason for this deviation, not considered so far, is the buoyancy of gas bubbles, which could cause unstable flow in the sample. Gas bubbles still are present in a small fraction after the foam rapidly collapses. They may not directly influence the feed viscosity, but may create instability during viscosity measurements.

A characteristic time scale for the rotating spindle is $t_m \sim O(\omega^{-1})$, whereas a time scale associated with the dynamics of the bubbles is

$$t_d \sim O\left(\frac{d}{2U_b}\right) = O\left(\frac{9\eta_0}{\pi g d\Delta\rho(1-\varphi_g)^n}\right) \quad (20)$$

where U_b denotes a characteristic velocity of the bubble due to buoyancy. Here, d, $\Delta\rho$, and g are a characteristic bubble size, the density difference between the continuous and gas phases, and the gravitational constant, respectively. The factor $(1-\varphi_g)^n$ originated from hindered settling in the presence of neighboring bubbles; n is ~4.65 when Stokes' law is valid.[35] Using $d \sim 0.1$ mm, $\Delta\rho \sim 2.6$ g/cm^3, and $\varphi_g \sim 0.4$ as reasonable estimates,[36] we obtain $t_d \sim 60$ s at 1100 °C, which is smaller than $t_m \sim 200$ s. In contrast, using $d \sim 1$ mm, $\Delta\rho \sim 2.6$ g/cm^3, and $\varphi_g \sim 0.7$ as reasonable estimates,[36] we obtain $t_d \sim 1200$ s at 900 °C, which is larger than t_m. This indicates that the dynamics associated with the bubbles is nearly pseudosteady at 900 °C. This simple scaling illustrates a possible instability in the measurement due to buoyancy. Note that the instability becomes more complicated considering the temperature difference between the spindle and crucible discussed previously.

Implication of Reacting Feed Viscosity on the Rate of Melting. As motioned in the Introduction, the foamy portion of the cold cap influences the melting rate by hindering heat transfer from the melt to the reacting zone. In the melter with

bubblers, vigorous forced convection within the melt pool not only brings hot melt to the cold cap, but also sweeps away "fining" bubbles ascending from the melt that otherwise would accumulate under the cold cap, creating a secondary foam layer. The question is to what extent strong convection can affect the primary foam. While the bubblers can expose the cold cap to hot melt around the vent holes, the addition of bubbling outlets does not directly result in additional openings in the cold cap.[37]

As Figure 7 indicates, the feed viscosity could be 30−50 Pa s at the cold-cap bottom (∼ 980−1000 °C). This viscosity is substantially higher than the viscosity of glass in the melt pool (∼ 5 Pa s). Because of its high viscosity and low density, the bottom layer of the cold cap is likely to resist the shear stress imposed by the circulating low-viscosity melt. Therefore, the best way of dealing with primary foam is to formulate the feed in such a way to prevent foaming. This would be possible if the gases from melting reactions could escape while the feed still possesses open porosity (i.e., before the glass-forming melt consolidates and becomes connected).

IMPLICATION FOR NUCLEAR WASTE VITRIFICATION

Cold-cap reactions produce a continuous glass-forming phase with suspended solid particles (quartz) and gas bubbles. As temperature increases and quartz particles dissolve, the glass-forming phase undergoes compositional changes. Consequently, along with temperature, the viscosity of the reacting melter feed is affected by the presence of solid particles, bubbles, and compositional inhomogeneity, and also by changes in the overall composition of the continuous phase, which is a consequence of solids dissolution. Analysis of these effects has shown that the volume fraction of dissolving quartz is dominant. It cannot be distinguished from the effect of gas bubbles because the gas-phase fraction and quartz fraction are not independent.

Quartz particles can be optimized to minimize foaming and produce uniform melt. By dissolving over a wide temperature range, quartz particles maintain the fraction of silica dissolved in the initial glass forming melt at a low level, thereby keeping a low glass-phase volume and delaying the closure of open pores. Open pores then allow gases to escape to atmosphere instead of being trapped in the melt and causing foaming.

Bubbling the melt can allow the cold cap to be well spread over the melt surface. Interestingly, not all melters produce cold cap. For example, in a stirred melter, the feed is mixed directly with molten glass.[38] Unfortunately, excessive foaming prevented industrial employment of such melter.

More than 200 000 m^3 of nuclear waste will be vitrified at the Hanford Site over the coming decades.[39] Understanding melter feed rheology is a key component for an enhanced mathematical model that estimates the melter waste-processing rates and guides strategies for efficient operations in the WTP[40] that will significantly shorten the life cycle of the cleanup process at the Hanford Site.

As a final note, we would like to emphasize that the current work was performed with one of hundreds of feeds anticipated for processing at the WTP. German, French, Korean, and other waste glass producers,[41,42] similar to the Defense Waste Processing Facility at the Savannah River Site, all premelt vitrification additives in the form of glass frit. As has been demonstrated,[43−46] feeds with glass beads (frit) may produce extensive foaming, both in low-viscosity frit that sinters early and in feeds with high-alkali wastes that attack frit particles at low temperature, causing early sintering and subsequent foaming similar to foam glass manufacturing.[47] Using raw materials (minerals and chemicals) for glass-forming and glass-modifying additives provides flexibility that allows optimization of feed for both different types of wastes and a stable fast-melting cold cap.

AUTHOR INFORMATION

Corresponding Author

*Phone: 509-372-6257; fax: 509-372-5997; e-mail: jaehun.chun@pnnl.gov.

Funding

This work was supported by the U.S. Department of Energy's Waste Treatment & Immobilization Plant Federal Project Office under the direction of Dr. Albert A. Kruger.

Notes

The authors declare no competing financial interest.

ACKNOWLEDGMENTS

We are grateful to Dr. Dong-Sang Kim and Jarrod Crum for insightful discussions/suggestions and to Jarrett Rice for the density measurements. Pacific Northwest National Laboratory is operated by Battelle Memorial Institute for the U.S. Department of Energy under contract DE-AC05-76RL01830.

REFERENCES

(1) Pokorný, R.; Hrma, P. Mathematical modeling of cold cap. *J. Nucl. Mater.* **2012**, *429*, 245−256.

(2) Hrma, P.; Kruger, A. A.; Pokorný, R. Nuclear waste vitrification efficiency: cold cap reactions. *J. Non-Cryst. Solids* **2012**, *358*, 3559−3562.

(3) Pokorný, R.; Pierce, D. A.; Hrma, P. Melting of glass batch: model for multiple overlapping gas-evolving reactions. *Thermochim. Acta* **2012**, *541*, 8−14.

(4) Smith, P. A.; Vienna, J. D.; Hrma, P. The effects of melting reactions on laboratory-scale waste vitrification. *J. Mater. Res.* **1995**, *10*, 2137−2149.

(5) Matyáš, J.; Hrma, P.; Kim, D.-S. *Melt Rate Improvement for High-Level Waste Glass*; PNNL-14003; Pacific Northwest National Laboratory: Richland, WA, 2002.

(6) Rodriguez, C.; Chun, J.; Schweiger, M. J.; Kruger, A. A.; Hrma, P. Application of evolved gas analysis to cold-cap reactions of melter feeds for nuclear waste vitrification. *Thermochim. Acta* **2014**, *592*, 86−92, DOI: 10.1016/j.tca.2014.06.022.

(7) Missimer, D.; Jurgensen, A.; Rutherford, R. *High Temperature X-Ray Diffraction Analyses of Simulated DWPF Sludge Batch 2 SRAT Products*; SRNL-L4200-2009-00029; Savannah River National Laboratory: Aiken, SC, 2009.

(8) Beerkens, R. G. C.; van der Schaaf, J. Gas release and foam formation during melting and fining of glass. *J. Am. Ceram. Soc.* **2006**, *89*, 24−35.

(9) Fedorov, A. G.; Pilon, L. Glass foams: formation, transport properties, and heat, mass, and radiation transfer. *J. Non-Cryst. Solids* **2002**, *311*, 154−173.

(10) Hrma, P.; Schweiger, M. J.; Humrickhouse, C. J.; Moody, J. A.; Tate, R. M.; Rainsdon, T. T.; Tegrotenhuis, N. E.; Arrigoni, B. M.; Marcial, J.; Rodriguez, C. P.; Tincher, B. H. Effect of glass-batch makeup on the melting process. *Ceramics − Silikáty* **2010**, *54*, 193−211.

(11) Schweiger, M. J.; Hrma, P.; Humrickhouse, C. J.; Marcial, J.; Riley, B. J.; TeGrotenhuis, N. E. Cluster formation of silica particles in glass batches during melting. *J. Non-Cryst. Solids* **2010**, *356*, 1359−1367.

(12) Shaw, D. J. *Introduction to Colloid and Surface Chemistry*; Butterworths: London, 1980.

(13) Denkov, N. D.; Tcholakova, S. S.; Höhler, R.; Cohen-Addad, S. Foam Rheology. In *Foam Engineering: Fundamentals and Applications*; Stevenson, P., Ed.; Wiley-Blackwell: Singapore, 2012; Chs. 6 and 7.
(14) Weaire, D. The rheology of foam. *Curr. Opin. Colloid Interface Sci.* **2008**, *13*, 171−176.
(15) Höhler, R.; Cohen-Addad, S. Rheology of liquid foam. *J. Phys.: Condens. Matter* **2005**, *17*, R1041−R1069.
(16) van der Schaaf, J.; Beerkens, R. G. C. A model for foam formation, stability, and breakdown in glass-melting furnaces. *J. Colloid Interface Sci.* **2006**, *295*, 218−229.
(17) Hrma, P. Effect of heating rate on glass foaming: Transition to bulk foam. *J. Non-Cryst. Solids* **2009**, *355*, 257−263.
(18) Hrma, P. Arrhenius model for high-temperature glass-viscosity with a constant pre-exponential factor. *J. Non-Cryst. Solids* **2008**, *354*, 1962−1968.
(19) Hrma, P.; Arrigoni, B. M.; Schweiger, M. J. Viscosity of many-component glasses. *J. Non-Cryst. Solids* **2009**, *355*, 891−902.
(20) Hrma, P. R.; Schweiger, M. J.; Arrigoni, B. M.; Humrickhouse, C. J.; Marcial, J.; Moody, A.; Rodriguez, C.; Tate, R. M.; Tincher, B. *Effect of Melter-Feed-Makeup on Vitrification Process*; PNNL-18374; Pacific Northwest National Laboratory: Richland, WA, 2009.
(21) Pokorný, R.; Rice, J. A.; Crum, J. V.; Schweiger, M. J.; Hrma, P. Kinetic model for quartz and spinel dissolution during melting of high-level-waste glass batch. *J. Nucl. Mater.* **2013**, *443*, 230−235.
(22) Bourova, E.; Richet, P. Quartz and cristobalite: High-temperature cell parameters and volume of fusion. *Geophys. Res. Lett.* **1998**, *25*, 2333−2336.
(23) Hrma, P.; Han, S.-S. Effect of glass composition on activation energy of viscosity in glass-melting temperature range. *J. Non-Cryst. Solids* **2012**, *358*, 1818−1829.
(24) Russel, W. B.; Saville, D. A.; Schowalter, W. R. *Colloidal Dispersions*; Cambridge University Press: New York, 1989.
(25) Hiemenz, P. C.; Rajagopalan, R. *Principles of Colloids and Surface Chemistry*, 3rd ed.; Marcel Dekker Inc.: New York, 1997.
(26) Llewellin, E. W.; Mader, H. M.; Wilson, S. D. R. The constitutive equation and flow dynamics of bubbly magmas. *Geo. Res. Lett.* **2002**, *29*, 23.
(27) Stevenson, P. *Foam Engineering: Fundamentals and Applications*; John Wiley & Sons: Singapore, 2012.
(28) Berg, J. C. *An Introduction to Interfaces & Colloids: The Bridge to Nanoscience*; World Scientific Publishing Co.: Hackensack, NJ, 2010.
(29) Henager, S. H.; Hrma, P. R.; Swearingen, K. J.; Schweiger, M. J.; Marcial, J.; TeGrotenhuis, N. E. Conversion of batch to molten glass, I: Volume expansion. *J. Non-Cryst. Solids* **2011**, *357*, 829−835.
(30) Steffe, J. F. *Rheological Methods in Food Process Engineering*; Freeman Press: East Lansing, MI, 1992.
(31) Crum, J. V.; Edwards, T. B.; Russell, R. L.; Workman, P. J.; Schweiger, M. J.; Schumacher, R. F.; Smith, D. E.; Peeler, D. K.; Vienna, J. V. DWPF startup frit viscosity measurement round robin results. *J. Am. Ceram. Soc.* **2012**, *95*, 2196−2205.
(32) Pokorný, R.; Hrma, P. Model for the conversion of nuclear waste melter feed to glass. *J. Nucl. Mater.* **2014**, *445*, 190−199.
(33) Bird, R. B.; Stewart, W. E.; Lightfoot, E. N. *Transport Phenomena*; John Wiley & Sons: New York, 1960.
(34) Shibata, H.; Suzuki, A.; Ohta, H. Measurement of thermal transport properties for molten silicate glasses at high temperatures by means of a novel laser flash technique. *Mater. Trans.* **2005**, *46*, 1877−1881.
(35) Richardson, J. F.; Zaki, W. N. Sedimentation and fluidization: Part I. *Trans. Inst. Chem. Eng.* **1954**, *32*, 35−53.
(36) Dixon, D. R.; Schweiger, M. J.; Hrma, P. R. Characterizing a high-level waste cold cap via elemental and structural configuration; *WM2014 Conference*, Paper 13362, Phoenix, AZ, 2014.
(37) Matlack, K. S.; Kot, W. K.; Callow, R. A.; Joseph, I.; Pegg, I. L. *Testing of Optimized Bubbler configuration for HLW Melter*; VSL-13R2950-1; Vitreous State Laboratory, The Catholic University of America: Washington, DC, 2014.
(38) Richards, R. S.; Jain, V. Rapid stirred melting of simulated West Valley high level waste. *Environmental Issues and Waste Management Issues in Ceramic Industries, Ceram. Trans.* **1994**, *39*, 119−238.
(39) Perez, J. M., Jr.; Barnes, S. M.; Morrey, E. V.; Kelly, S., Jr.; Petkus, L. Vitrification testing and development for the Hanford waste treatment and immobilization plant. *Environmental Issues and Waste Management Technologies X, Ceram. Trans.* **2004**, *168*, 3−20.
(40) Matyáš, J.; Hrma, P.; Kim, D.-S. Analysis of feed melting processes. *Environmental Issues and Waste Management Technologies IX, Ceram. Trans.* **2003**, *155*, 69−78.
(41) Vienna, J. D. Nuclear waste vitrification in the United States: Recent developments and future options. *Int. J. Appl. Glass Sci.* **2010**, *1*, 309−321.
(42) Jantzen, C. M.; Lee, W. E.; Ojovan, M. I. Radioactive Waste conditioning, immobilization, and encapsulation processes and technologies: overview and advances. In *Radioactive Waste Management and Contaminated Site Clean-up: Processes, Technologies and International Experience*; Lee, W. E., Ojovan, M. I., Jantzen, C. M., Eds.; Woodhead Publishing: Oxford, 2013; Ch. 6.
(43) Anderson, L. D.; Dennis, T.; Elliott, M. L.; Hrma, P. Waste glass melting stages. *Ceram. Trans.* **1994**, *39*, 213−220.
(44) Kim, D. S.; Hrma, P. Laboratory studies for estimation of melting rate in nuclear waste glass melters. *Ceram. Trans.* **1994**, *45*, 409−419.
(45) Watanabe, K.; Yano, T.; Takeshita, K.; Minami, K.; Ochi, E. X-ray CT imaging of the vitrified glasses containing pseudo-radioactive wastes - Structure and chemical reactions of glass beads and wastes in cold cap. *Glass Technol.: Eur. J. Glass Sci. Technol., Part A* **2012**, *53*, 273−278.
(46) Choi, A. S.; Miller, D. H.; Immel, D. M. *Determination of HLW Glass Melt Rate Using X-Ray Computed Tomography (CT)*; SRNL-STI-2010-00767; Savannah River National Laboratory: Aiken, SC, 2011.
(47) Carter, C. B.; Norton, M. G. *Ceramic Materials*; Springer: New York, 2013.